NASA
Technical
Paper
2551

March 1986

New Technique for Experimental Generation of Two-Dimensional Blade-Vortex Interaction at Low Reynolds Numbers

Earl R. Booth, Jr.,
and James C. Yu

NASA

New Technique for Experimental Generation of Two-Dimensional Blade-Vortex Interaction at Low Reynolds Numbers

Earl R. Booth, Jr.,
and James C. Yu

Langley Research Center
Hampton, Virginia

Summary

An experimental investigation of two-dimensional blade-vortex interaction was initiated at NASA Langley Research Center. The first phase of this investigation was a flow visualization study to document the approach process of a two-dimensional vortex as it encountered a loaded blade model. To accomplish the flow visualization study, a method for generating two-dimensional vortex filaments was required. This report documents the numerical study used to define a new vortex generation process and the use of this process in the flow visualization study. Additionally, photographic techniques and data analysis methods used in the flow visualization study are examined.

Introduction

Blade-vortex interaction (BVI) occurs in a helicopter rotor when the trailing vortex from one rotor blade comes into close proximity or actually collides with a rotor blade. Under certain conditions, this encounter causes an impulsive aerodynamic load on the rotor blade that may be radiated as low-speed BVI noise. Low-speed BVI is a dominant noise source when it occurs. Extensive study of BVI noise generation is currently being pursued by several groups in the aeroacoustics community (refs. 1–8).

Analytically, the acoustic formulation for low-speed BVI noise is fairly well developed; however, the detailed aerodynamic input required by the acoustic formulation is seriously deficient. Widnall (ref. 1) linked the angle of intersection, measured between the axis of rotation of the vortex and the blade span, to the amplitude and duration of the pulse produced by the encounter such that when the intersection angle is zero, the most intensive pulse is produced. Nakamura (ref. 2) reached a similar conclusion and emphasized the importance of the leading-edge region of the blade in the interaction process. Thus, the limiting case representing the most intense noise generation occurs when the intersection angle between the vortex and the blade is zero. This case is labeled two-dimensional BVI, since the geometry of the encounter can be modeled as a two-dimensional vortex encountering an airfoil.

Experimentally, Hoad (ref. 3) demonstrated that the most intense BVI acoustic radiation is generated in the first quadrant of the rotor disk. This result is supported by the earlier work of Tangler (ref. 4), in which the BVI encounters that generated the most noise were also located in the first quadrant. Recent numerical work by Egolf and Landgrebe (ref. 5) on the structure of the rotor wake shows the first quadrant to contain vortices in a nearly parallel orientation to the rotor blades for operating conditions under which BVI noise occurs. However, this study concludes that more experimental work is needed concerning the detailed process of the encounter between a vortex and a rotor blade.

Low-speed two-dimensional blade-vortex interaction has been studied numerically. Hardin and Mason (ref. 6) used an inviscid point vortex to investigate low-speed BVI and concluded that a fully viscous study would be required to completely model the phenomenon. Hardin and Lamkin (ref. 7) used the unsteady, fully viscous Navier-Stokes equations in a study involving the encounter between a Joukowski airfoil and a distributed vortex. Although the study was limited to very low Reynolds numbers because of computational limitations, results indicate that viscous effects, particularly vortex core distortion and displacement, are of primary importance in the sound generation process of BVI noise.

An experimental flow visualization study of two-dimensional BVI, limited to low-subsonic flows, was conducted by Booth and Yu (ref. 8). The study indicates that distortion of the vortex core is an important feature of the close encounter case, and that the nature of the interaction is chiefly dependent on the vertical separation distance between the blade and the vortex. Since the vortex core is a viscous phenomenon, the experimental study provides detail that is not included in inviscid numerical methods. Comparison of results with the viscous numerical study of Hardin and Lamkin shows qualitative agreement on details of the interaction process. The vortex generation method employed in the flow visualization study is the object of this report.

It should be mentioned here that at least two other transverse vortex generation methods have been used with success. Commerford and Carta (ref. 9) used the wake of a cylinder to create a high-reduced-frequency flow field for their measurement of unsteady lift. Ziada and Rockwell (ref. 10) used the roll-up of the shear layer formed between two streams of different velocity to produce the vortex filaments for their vortex-leading-edge studies.

Symbols

The coordinate system used in this study is presented in figure 1.

$A(k)$ real portion of pitching oscillation transient lift function

a distance to axis of rotation measured from leading edge of oscillating airfoil, $c/4$

$B(k)$ imaginary portion of pitching oscillation transient lift function

C	blade model chord length, 8 in.	Y_b/C	vertical distance between vortex and blade
$C(k)$	Theodorsen transient lift function		
c	vortex generator chord length, 6 in.	z	height above reference level
c_l	section lift coefficient, l/qc	α	angle of attack for blade model
$F(k)$	real portion of Theodorsen function $C(k)$	α_g	angle of attack for vortex generator
		θ	angle of inclination of oscillating airfoil
f	focal length of camera system	ν	kinematic viscosity
$G(k)$	imaginary portion of Theodorsen function $C(k)$	ρ	density
		ω	circular frequency of oscillation

k reduced frequency, $\omega c/2U$

A dot over a symbol denotes the derivative with respect to time.

L_b	distance between background plane and focus of camera system
L_f	distance between foreground plane and focus of camera system
L_m	distance between midspan plane and focus of camera system
l	section lift
q	dynamic pressure, $\rho U^2/2$
R	vortex core radius
r	distance from line of symmetry to given point (x, y)
r_b	distance from line of symmetry to image of (x, y) from background plane
r_f	distance from line of symmetry to image of (x, y) from foreground plane
r_m	distance from line of symmetry to image of (x, y) from midspan plane
t	age of vortex
U	free-stream velocity
$w(x)$	relative downward velocity of oscillating airfoil
X	x-coordinate in experimental coordinate system
X/C	nondimensional x-coordinate in experimental coordinate system
x	distance measured from leading edge of blade model
Y	y-coordinate in experimental coordinate system
Y/C	nondimensional y-coordinate in experimental coordinate system

Generation of Transverse Vortices

Blade-vortex interaction is a three-dimensional unsteady aerodynamic phenomenon that occurs in a translating rotor under a certain set of operating conditions. Studies of BVI using rotor models in wind tunnels and helicopters in flight tests have yielded considerable insight into the problem. However, in order to understand the mechanism by which this aerodynamic phenomenon causes BVI noise, it is necessary to experimentally examine some simpler cases. Two limiting cases of BVI defined by the intersection angle between the vortex and the blade are the normal incidence case, in which the vortex is perpendicular to the blade, and the two-dimensional case, in which the vortex is parallel to the blade. The former case is a steady three-dimensional problem which yields the shape of the steady-state vortex as it bends around the blade. The latter is an unsteady two-dimensional problem which yields vortex trajectory, convection velocity, vortex core distortion, and the unsteady loading on the blade in a geometry similar to the three-dimensional BVI case for which the most intense sound is generated. However, the latter experiment is much more difficult to perform primarily because generation of a vortex perpendicular to the velocity vector is more difficult. The purpose of this report is to document how such vortices were generated and used to produce two-dimensional blade-vortex interaction experimentally.

Characteristics of the vortex wake produced by oscillating an airfoil about its quarter-chord were studied numerically to determine if transverse vortices suited to the study of two-dimensional blade-vortex interaction could be produced by this process. From the analysis, the vortex generation process was determined to be governed by two key parameters: reduced frequency and oscillation amplitude. Reduced frequency ($\omega c/2U$) is, essentially, a ratio of the oscillation rate, ω, to the test section

velocity, U, such that vortex roll-up is enhanced at high reduced frequency. In other words, vortex roll-up is proportional to the oscillation rate and inversely proportional to the test section velocity. Oscillation amplitude was found to enhance vortex roll-up and to yield vortex roll-up at lower reduced frequencies. However, since the analysis included no viscous effects (such as dynamic stall of the vortex generator blade), the maximum oscillation amplitude considered in the analysis was limited to less than the static angle of stall for the vortex generator airfoil.

The analysis was extended to examine the effect of nonsinusoidal oscillation on vortex wake structure with the objective of producing a single well-developed vortex per cycle, rather than the paired vortices produced by sinusoidal oscillation. This single vortex simulates more closely the isolated BVI encounter, in which the distance between vortices is greater than the blade chord. For sinusoidal oscillation, the distance between vortices of like sign decreases with increasing reduced frequency, so that at the nominal test conditions, the distance is on the order of 1 blade chord length. The goal of the nonsinusoidal pitch schedule was to increase this distance to 5 chord lengths. The nonsinusoidal pitch schedule selected for use in the first phase study was developed from a sawtooth wave.

The nonsinusoidal pitch schedule, consisting of a sinusoidal sweep from the minimum to the maximum angle of attack of the vortex generator blade during the first 20 percent of the cycle and a linear return sweep back to the initial minimum angle of attack during the remaining 80 percent of the cycle, was used to generate an asymmetric wake pattern. Figure 2 is a plot of the nonsinusoidal pitch schedule. It was hoped that a concentrated single vortex would be produced during the rapid sinusoidal segment of the oscillation, followed by a diffused vortex sheet produced by the linear return sweep. For this type of pitch schedule, vortex spacing can be controlled by varying the relative lengths of the rapid sinusoidal sweep and the longer relaxation portions of the cycle.

The wake produced by an airfoil pitching about its quarter-chord location was numerically studied by using a discrete vortex method. Implicit in the formulation of the method employed to simulate the process of vortex wake generation is the assumption of quasi-steadiness, in that the process can be broken down into a series of time steps. Essentially, the simulation proceeded as follows:

1. The pitch schedule was input and decomposed into its Fourier components to calculate the transient lift as a function of oscillation phase angle only. This step was not necessary for sinusoidal pitch schedules with only one frequency component but was required for the nonsinusoidal pitch schedule.

2. Airfoil angle of attack (α_g) and rate of positional change $(\dot{\alpha}_g)$ were computed from the given pitch schedule.

3. The value of the transient lift was computed by using the Fourier components calculated in step 1.

4. The circulation about the airfoil, represented as a vortex located at the quarter-chord location, was calculated.

5. A vortex of strength equal to the change in circulation since the last time step, but opposite in sign, was released at the current position of the airfoil trailing edge.

6. For each of the previously released vortices, the position of the individual vortex was updated by calculating the induced velocity from every other vortex in the domain (including circulation about the airfoil) at the old location, adding the free-stream velocity to the induced velocity, and multiplying by the time difference to obtain the new location.

7. The time counter was incremented, tested to see if it exceeded the maximum time for the calculation, and returned to step 2 if the maximum time had not been exceeded.

8. At the end of the calculation, the location and strength of each of the vortices in the wake were output to a computer data file for plotting. Two key features of the simulation were the transient lift functions and the vortex influence functions. The first determines the strength of each of the vortices in the wake, and the latter determines how the individual vortices move in the wake. Discussion of these key elements completes the description of the vortex wake analysis.

Transient Lift Functions

One of the key elements of the code was the transient lift functions. The source for these functions was Theodorsen's classical work on flutter (ref. 11) and the extension of that work by Sears (ref. 12). Essentially, the transient lift is calculated as a function of the reduced frequency of the oscillation. Although the specific type of oscillation described in reference 11 is plunging of the airfoil, reference 12 contains a derivation of the lift functions that can be modified to represent oscillation in pitch about

the quarter-chord, the case desired for the present purpose.

A lift function can be obtained from the differential equation in reference 12

$$w(x) = \left[\theta U - \dot{z} + \left(\frac{c}{z} - a\right)\dot{\theta}\right] + \dot{\theta}x \qquad (1)$$

and the geometry in figure 3. The lift function thus derived is

$$c_l(\alpha_g, \dot{\alpha}_g, k) = 2\pi \left[\alpha_g\, A(k)\; +\; \dot{\alpha}_g \frac{c}{2U}\, B(k)\right] \qquad (2)$$

where

$$\left.\begin{array}{l} A(k) = F(k) - k\,G(k) - \dfrac{k^2}{4} \\[2mm] B(k) = F(k) + \dfrac{G(k)}{k} + \dfrac{1}{2} \end{array}\right\} \qquad (3)$$

The symbols $F(k)$ and $G(k)$ represent the real and imaginary parts of the complex Theodorsen function $C(k)$, and k is the reduced frequency of the oscillation.

The lift function in equation (2) was coded as a subroutine. This coding technique allowed relatively simple comparison of the effect of various lift functions on the wake structure. The wake geometry solution was similar for the lift function described above, the Theodorsen lift function, and the Sears lift function. The reason for this is purely numerical because for very small time steps, the change in lift, which determines the strength of each of the released vortices in the wake, is a small number. Minor variations in the magnitude of each of the small numbers tend to be insignificant when the global structure of the wake is considered.

Vortex Influence Functions

The second key element of the simulation algorithm was the vortex influence functions. Since this portion of the code is executed for each vortex during each time step, it is the principal element determining computation time and, hence, resolution. For this reason, computational efficiency was an important consideration in the algorithm chosen.

For any given vortex in the wake at any given moment, an induced velocity acts at the location in space occupied by the vortex. This induced velocity is the sum of the velocities induced by the circulation about the airfoil and each of the other vortices in the wake. After a given time increment, the vortex will have moved a distance to a new location determined by the time integration of the induced velocity at the center of the vortex as it moves to the new location. For sufficiently small time intervals, the distance and

direction of the vortex movement are approximately equal to the product of the time interval and the total induced velocity. Thus, for small time steps, the new position of a vortex can be calculated by summing the induced velocity from each vortex in the domain on the vortex of interest and multiplying by the time difference.

For most cases, the calculation of the wake geometry consisted of the above procedure for each vortex in the wake. However, for cases in which two vortices are very close to each other, using the simple inviscid vortex model yields very large induced velocities as a result of the velocity singularity at the center of the vortex. The result is a vortex excursion that is not a feature of the real flow being simulated. In order to solve this problem, it was necessary to introduce a merging function, so that as the vortices drift together, they merge into a single vortex with a strength equal to the sum of the circulation of the two vortices. Not only does this method promote numerical stability in the calculation, but it reduces the number of wake vortices that have to be considered and incrementally speeds up the calculation.

In order to implement the merging routine, definition of a critical radius was needed. Since the classical inviscid vortex velocity model is representative of a vortex field outside of the vortex core, the vortex core radius was selected as the critical radius. From the Prandtl analysis (ref. 13), the radius of the vortex at a given time t after its creation is given by

$$R = \sqrt{4\nu t} \qquad (4)$$

where ν is the kinematic viscosity. The calculation requires that the age of each vortex, t, must be known, and therefore, stored. It was observed that the vortices move in the downstream direction at approximately the free-stream velocity. Therefore, it is assumed that the age of the vortex is approximately the time calculated by dividing the x-coordinate of the vortex by the free-stream velocity. Thus, an approximate critical radius of the vortex can be calculated from its position.

The process of wake geometry update, then, proceeded as follows: For every vortex released in previous time steps,

1. A critical radius was calculated.
2. For vortices outside of the critical radius, an induced velocity was calculated at the present location of the vortex and added to previously calculated induced velocities.
3. For vortices inside of the critical radius, the strength of the combined vortex was computed.
4. A new location was computed and stored in a temporary array along with the vortex strength.

After the last vortex in the wake was updated, the temporary array holding the new wake geometry replaced the "permanent" wake geometry array, and the temporary array was cleared. The calculation proceeded as indicated above until the maximum time for the calculation was reached, at which time the wake geometry, in the form of the position and strength of each of the vortices in the wake, was stored on a data file.

Sample Results From Calculation

Two cases of particular relevance to the experimental investigation are sinusoidal oscillation at a frequency of 30 Hz and an amplitude of 10° and nonsinusoidal oscillation at a frequency of 6 Hz and an amplitude of 10°. The first case represents the nominal operating conditions for the vortex generator, and the second represents the nonsinusoidal case in which the secondary structure appeared in the experiment. The results of the calculation are presented in the form of wake maps, where the position of each vortex is plotted with a symbol size proportional to the strength of the vortex. This particular representation is used to examine the kinematic structure of the wake and is qualitatively similar to the flow visualization picture obtained experimentally. Figures 4 and 5 consist of wake maps and corresponding flow visualization pictures for the two cases mentioned above.

In figure 4(a), a wake map representing the sinusoidal case is presented. The shape of the data symbol represents the rotational direction of the vortex, and the size of the data symbol is proportional to the strength of the vortex element. A positive vortex rotates in the clockwise direction. From the wake map, the major vortices, represented by the closely spaced groups of vortex elements, alternate in sign, with the negative vortex groups at positive values of Y/C. From a corresponding flow visualization picture in figure 4(b), the same vortex group features are evident as vortex filaments. Note especially the organization of the positive vortex located around $(0.75, -0.25)$ as compared with the organization of the positive vortex at $(1.9, -0.12)$ and the corresponding flow features in the photograph. In this sense, the code enabled viewing of the vortex wake flow field before any of the hardware for the actual test was built.

In figure 5(a), a wake map from the nonsinusoidal oscillation case is presented. Figure 5(b) is a photograph from the experiment showing the flow field at an earlier phase angle. Although the correspondence between the wake map and the photograph is weaker here because of the presence of the blade model and the phase angle mismatch, the main features of the wake are preserved in each. In the wake map, the wake is composed of a small positive vortex located at $(1.25, 0.30)$ and a larger elongated negative vortex. In the photograph, the larger negative vortex is shown as it encounters the blade leading edge. Notice the group of smaller secondary vortices in the photograph. This secondary structure in the wake corresponds to the weaker positive vortex group.

The discrete vortex approximation has been applied to the problem of an airfoil pitching about its quarter-chord location to serve as a design tool for the vortex generator. It has been shown to produce wake maps that compare well with flow visualization photographs obtained in the experimental study. Thus, discrete vortex approximation provided a model sufficiently accurate to study the major flow fields produced by the vortex generation process.

Overview of Experiment

The two-dimensional BVI flow visualization study was conducted in the Quiet Flow Facility in the Langley Aircraft Noise Reduction Laboratory, described in reference 14. The low-pressure air system was used to provide the flow to the experimental apparatus. The test section consists of two side plates attached to the long sides of a 1.5- by 1.0-ft rectangular nozzle. A sketch and a photograph of the test apparatus are presented as figure 6. Inside the test section, the vortex generator, an oscillating airfoil, was located downstream of the nozzle exit. The vortices generated were allowed to interact with a blade model positioned in the test section by a sting/traverse system.

Test conditions were monitored from a computer terminal. For instance, flow speed in the test section was measured by a pitot-static probe located at the nozzle exit. Other conditions monitored included barometric pressure and temperature of the flow in the test section. Interactive software also controlled the traverse and photographic systems.

Observation windows in the side plates allowed photography of the flow. The vortex wake was seeded with smoke emitted from the vortex generator. The test section was illuminated by two banks of strobe lights located on opposite sides of the test section. With the period of oscillation of the vortex generator as a time reference, the strobe lights were triggered at specified oscillation phase angles. Phase-locked photography was employed to record the flow with a high-resolution still camera by making multiple photographic exposures at a given phase angle. Additionally, slow-scan video photography employed the interface board to advance the phase angle illuminated by successive flashes and produced a

slow-motion dynamic record of the interaction process. The phase-locked photography was used primarily as the source for the trajectory data extraction, whereas the slow-scan video was primarily useful in observing the qualitative details of the dynamic process.

Vortex Generator

The vortex generator consisted of an NACA 0012 airfoil model with a 6-in. chord driven in pitch oscillation about its quarter-chord station to a maximum frequency of 30 Hz with a maximum amplitude of 10° about a nominal mean angle of attack of 0°. The vortex generator was driven by an electric 0.5-horsepower motor through a captured cam transmission. Oscillation rate was controlled by varying motor speed. Interchangeable cams were used to vary oscillation pitch schedule and amplitude. Cams producing sinusoidal oscillation with amplitudes of 1°, 5°, and 10° and nonsinusoidal oscillation with an amplitude of 10° were tested. Mean angle of attack was varied by a set of interchangeable cam follower arms with offsets of 0°, 5°, and 10°.

Satisfactory vortex roll-up in the wake created by the vortex generator was observed experimentally only for the sinusoidal oscillation case at an amplitude of 10° and a frequency of 30 Hz. The flow speed was 20 feet per second. Mean angle of attack had only a minor effect on the wake pattern, so the follower arm with an offset of 0° was used. These conditions were the nominal vortex generator operating conditions for the experiment.

The vortex generator blade was ducted to emit smoke particles from a small port in the midspan trailing edge. The smoke passage was routed through the main vortex generator blade shaft, on the side opposite the drive train, to the midspan, where the smoke was turned through an angle of 90° into a small tube (inner diameter of 0.125 in.) buried in the foam core of the blade that gradually flattened as it approached the exit port in the trailing edge. The smoke exit port is 0.25 in. wide and 0.035 in. high.

Rotor Blade Section Model

To simulate a rotor blade in the two-dimensional encounter, an airfoil model spanning the width of the test section was used. The airfoil model had an 8-in. chord and an NACA 0012 profile. The model, manufactured of solid aluminum, was mounted on a sting by a locking pivot to provide a means of varying blade angle of attack. The blade/sting assembly was positioned in the test section by a computer-controlled traverse system capable of positioning the

blade anywhere in the two-dimensional test section. Thus, the position of the blade model is a function of the three variables X, Y, and α. If the space variables are normalized with respect to blade chord length, blade position is completely defined by the coordinates α, X/C, and Y/C.

Photographic Techniques

Two main photographic techniques were employed to record the time-dependent flow patterns: phase-locked still photography and slow-scan video photography. Sample data obtained by both methods are presented in the section entitled "Sample Results From Experiment." An interface board used the signals from an optical encoder mounted on the vortex generator drive motor and computer commands from the data acquisition software to control the strobe lights and (in the case of phase-locked photography) the operation of the camera shutter.

A 70-mm camera with remote shutter triggering and automatic film advance was used for the phase-locked photography. The advantages of this photographic technique are twofold: first, the image on the film plate is built up over several cycles and allows photography of low-light-level smoke flows, and second, since the image is a composite of several cycles, an average image is produced (i.e., features that appear in all cycles are reinforced, but random variations tend to be averaged out). The number of exposures used in the phase-averaging process varied from 5 to 20, with best results achieved with approximately 15 exposures, since this produced best contrast between the dominant flow pattern and the blurring caused by random variations.

Photographs were taken at a series of phase angles evenly spaced throughout the oscillation cycle. Typically, 10 frames per cycle were recorded. A digital counter, visible in the photographic frame, was used to catalog the photographs. During the data acquisition process, the phase angle and corresponding frame number were recorded in a computer data file along with flow conditions measured before and after the photograph was taken. These data were used to ensure that the flow conditions were at the test point for each photograph.

Slow-scan photography, using a highly sensitive video camera capable of imaging in low-light, low-contrast conditions, was also accomplished by using the interface board. Operation of the hardware was nearly identical to that described above except that the shutter control function was disconnected. Slow-motion effects (a motion reduction factor of 500:1) could be accomplished by advancing the encoder count by one count, firing the strobe for one cycle, advancing the encoder count by one more count,

and so forth. In the test, the encoder count was incremented by 10, and each selected phase angle was used for 10 cycles. Thus, slow-motion photography with this system was reduced to a single simple DO loop in a data acquisition software routine.

The ability to record the process dynamically with the video camera proved invaluable for interpretation of the complex flow features and processes during the interaction. In addition, the video images are free from the blurring inherent in the phase-locked photographic process. Thus, examining the video records frame-by-frame allows an evaluation of exactly what sort of features are averaged out in the phase-locked process and provides an unblurred view of the process.

Analysis of Optical Data

Vortex trajectory was determined by mapping the vortex location from the photographic coordinate system to the experimental coordinate system for a series of phase-locked photographs taken during a cycle of vortex generator oscillation. Although the technique using a graphics table for measuring locations from a photograph is fairly standard, the coordinate transformation is not. Therefore, the coordinate transformation method is described in detail.

To simplify the mapping process, the following assumptions were made: (1) linear optical ray theory is applicable, (2) the film plane is parallel to the experimental plane, and (3) the center of the photographic print coincides with the center of the image. With these assumptions, the problem reduces to correcting for linear perspective.

In figure 7, a ray diagram for the experimental configuration is presented for an observer located downstream of the test chamber. The two side plates are labeled as front and back with respect to the camera location. Notice that the plane of interest is the midspan plane, where the vortex features we wish to track are rendered visible by the smoke particles. By drawing the optical ray path from given (x, y) locations in the three planes of interest, it can be seen immediately by similar triangles that the following ratios are constant and can be used as conversion factors in the mapping process:

$$\left.\begin{array}{l} \dfrac{r}{r_b} = \dfrac{L_b}{f} \\[2mm] \dfrac{r}{r_m} = \dfrac{L_m}{f} \\[2mm] \dfrac{r}{r_f} = \dfrac{L_f}{f} \end{array}\right\} \tag{5}$$

where the subscripts b, m, and f refer to the back side plate plane, the midspan plane, and the front side plate plane. The distance f is the focal length of the optical system.

Values of the conversion ratios are obtained by means of registration points. A registration point is a point in space whose location is known in both coordinate systems, for instance, the upper right-hand side of the window in the back side plate. From the registration points, the values for the first and third ratios can be computed directly. There are no registration points in the midspan plane, so solution for the second ratio is not as trivial.

The value of the second ratio can be found as follows: Consider the distance between the side plates, $L_b - L_f$. Setting this distance equal to $2q$ and rewriting the distances from the side plates to the focal point in terms of $L_f + nq$, where $n = 2$, 1, and 0 for the background, midspan, and foreground planes, respectively, allows solution for the focal distance f. Once this distance is found, the value of the midspan ratio can be determined directly.

Once the values of the conversion ratios are found, the measured locations from the photographic frame are converted to polar coordinates relative to an origin at the center of the image. These polar coordinates are then converted to the experimental coordinate system by use of the conversion ratios. Finally, the coordinates are converted to Cartesian coordinates, which are checked by means of the registration points. The chord length of the blade model was computed with an error of less than 3 percent.

Location data from a sequence of photographs taken during a cycle were processed as a set to produce vortex trajectory data. The trajectory data were used to deduce the trajectory perturbations of the vortices as a function of blade position and loading. Reference 8 was based on a systematic study of this trajectory data.

Sample Results From Experiment

A representative sampling of the results obtained in the study is presented here for completeness. For convenience, the results are divided into two parts corresponding to results obtained with sinusoidal and nonsinusoidal oscillation of the vortex generator.

Sinusoidal oscillation case. Figure 8 is a collection of a set of phase-locked photographs from a typical data run. The photographs, equally spaced 36° apart in the cycle, show the evolution of the vortex structures as they traverse the test section. Vortex trajectory data obtained from the photographs are plotted in figure 9. Each data point represents a location derived from a frame in figure 8. Such trajectory

data can be directly compared with data representing another test condition as in figure 10, which illustrates the effect of blade vertical separation distance on vortex trajectory. Analysis of such data led to the characterization of the blade-vortex interaction close encounter region as consisting of several interaction zones depending on the nature of the encounter, as illustrated in figure 11.

The phase-locked photographs were useful for quantifying the trajectory of the vortices as they encountered the blade, and the video records proved to be valuable in observing the fine detail of the interaction process. Figures 12–14 illustrate the interaction of a positive vortex with the blade, representative of an advancing side encounter, in each of the three interaction zones. The figures also illustrate the various types of encounters of the blade with the negative vortex. It should also be noted that the blade is at an angle of attack of 10° in all three figures.

In figure 12, the interaction of the vortices in the wake with the blade is recorded in the deflection zone with respect to the positive vortex. Blade position for this figure was (10°,0.75,0.25). In frame A, the negative vortex is shown in the instant before it collides with the blade. Frame B shows a separation zone on the upper surface of the airfoil apparently induced by the negative vortex as the vortex core rolls underneath the blade leading edge in a distortion zone encounter. Note the severe elongation of the negative vortex core. The positive vortex appears on the left side of the frame. Frame C illustrates the advance of the positive vortex as the separation region clings to the upper surface of the blade. Frame D shows the positive vortex continuing to advance toward the blade while the core size of the vortex expands. As the positive vortex reaches the blade (frame E), the core becomes oval in shape and is deflected away from the blade. The positive vortex, however, remains substantially organized as it passes underneath the blade, as shown in frame F. Note the appearance of the negative vortex in frame F as the cycle closes. In this deflection zone encounter of the positive vortex, the vortex structure is relatively undisrupted, but its trajectory is altered by the blade.

In figure 13, the blade has been moved to (10°,0.75,0.219), bringing the positive vortex into the fringes of the distortion zone. In frame A, the negative vortex is poised for a collision encounter with the blade. Frame B shows the disruption of the negative vortex and the separation region apparently induced on the upper surface of the blade by this encounter. Note that the disruption of the flow over the upper surface of the blade is more violent and shorter lived than the case recorded in figure 12. The positive vortex enters the frame on the left in frame B of fig-

ure 13 and advances toward the blade in frame C. The expansion of the positive vortex core is shown in frame D. Notice that the core is expanded to a greater extent than shown in frame D of figure 12. Once again, the vortex core takes an elliptical shape as it passes below the blade leading edge in frame E of figure 13. In this case, however, the orientation of the elliptical core is rotated counterclockwise. This apparent rotation is continued in frame F and gives the appearance of an elongation of the vortex core. As a result, the positive vortex core shown in frame F is flatter vertically than the positive vortex core shown in frame F of figure 12.

In figure 14, the blade has been moved to (10°,0.75,0.00). The flattening of the negative vortex core is illustrated in frames A and B as the vortex passes over the blade in a distortion zone encounter. The positive vortex enters in frame B with a core size noticeably greater than those illustrated in frame B of figures 12 and 13. The expansion of the vortex core continues in frames C and D of figure 14 as the vortex advances toward a collision zone encounter shown in frame E. In frame E, the positive vortex core is shown to split into two smaller vortex cores, one of which attempts to pass over the blade, the other beneath. The positive vortex pair is then shown to cling to the blade leading edge in frame F. This deceleration of the positive vortex and the unsteady loading on the blade resulting from the disruption of the positive vortex core in the collision zone encounter are believed to be the major noise-producing mechanisms for low-speed BVI noise (ref. 7).

Nonsinusoidal oscillation case. The interaction of the blade with the wake produced by sinusoidal oscillation of the vortex generator is shown to reveal much of the detail of the encounter of a blade with a vortex filament; however, it is desirable to increase the separation distance between the vortex filaments to eliminate vortex-vortex influences from the interaction process. As mentioned earlier, the most feasible method of accomplishing this objective was to modify the oscillation pitch schedule of the vortex generator.

The vortex generator was oscillated nonsinusoidally in an attempt to produce a single vortex filament for better simulation of an isolated blade-vortex encounter. Although a single vortex was indeed produced by this method, it was followed in the wake by a series of smaller secondary vortices instead of the diffuse vortex sheet desired. The interaction of the blade with the wake produced by the nonsinusoidal oscillation is presented as a sequence of phase-locked photographs in figure 15. The letters on each frame in figure 15 correspond to the labeled points

8

on the pitch schedule plot in figure 16. In frame A of figure 15, the smoke trail from the linear return stroke is evident. In frame B, the beginning of the vortex roll-up is shown, and in frame C, the vortex formation process is nearly complete. Frame D shows the single vortex moving away from the vortex generator at the beginning of the linear return stroke. Frames F through H show the development of the secondary vortex structure as it travels past the blade model. In frame I, the secondary vortex structure dissipates as it exits from the test section and thus completes the cycle. Further work is required to suppress the secondary vortex structure in order to more fully simulate the "isolated encounter" with this process.

Concluding Remarks

To study the detailed process of two-dimensional vortex generation, a discrete vortex method was used to conduct a numerical study of the aerodynamics of a pitching airfoil. The study showed that fully developed vortex filaments could be generated at reasonable operating conditions of a vortex generator. Vortex formation was shown to depend primarily on oscillation rate and amplitude. From information gained in this study, a vortex generator was designed and built.

Two-dimensional blade-vortex interaction was generated experimentally at low Reynolds numbers by using the wake of an oscillating airfoil to generate two-dimensional vortex filaments orthogonal to the test section velocity vector. The vortices and their interaction with a stationary blade model were studied by means of flow visualization techniques. The vortices generated and their interaction with a blade model were recorded by phase-locked and slow-scan photography.

The data obtained from the flow visualization study by the two photographic techniques yielded useful information concerning two-dimensional blade-vortex interaction. From the phase-locked photography, quantitative vortex trajectory data were obtained. While this information was useful in characterizing the global nature of the interaction process, the details of the interaction process were observed from the video records. The combination of the qualitative and quantitative information resulted in a generalized characterization of the interaction process.

Useful results have been obtained by using the transverse vortex generation process to create two-dimensional blade-vortex interaction experimentally. At present, qualitative flow visualization data have been obtained. Further research is required to measure blade surface pressure loading and other data

necessary to fully understand the blade-vortex interaction noise generation process.

NASA Langley Research Center
Hampton, VA 23665-5225
December 5, 1985

References

1. Widnall, Sheila: Helicopter Noise Due to Blade-Vortex Interaction, *J. Acoust. Soc. America*, vol. 50, no. 1 (pt. 2), July 1971, pp. 354–365.

2. Nakamura, Yoshiya: Prediction of Blade-Vortex Interaction Noise From Measured Blade Pressure. Paper No. 32, *Seventh European Rotorcraft and Powered Lift Aircraft Forum, Volume 1*, Deutsche Gesellschaft fur Luft- und Raumfahrt e. V., Sept. 1981.

3. Hoad, Danny R.: Helicopter Model Scale Results of Blade-Vortex Interaction Impulsive Noise as Affected by Tip Modification. *36th Annual Forum, American Helicopter Soc., Inc.*, May 1980, pp. 80-62-1– 80-62-13.

4. Tangler, James L.: Schlieren and Noise Studies of Rotors in Forward Flight. *33rd Annual National Forum, American Helicopter Soc., Inc.*, May 1977, pp. 77.33-05-1– 77.33-05-12.

5. Egolf, T. Alan; and Landgrebe, Anton J.: Helicopter Rotor Wake Geometry and Its Influence in Forward Flight. *Volume I—Generalized Wake Geometry and Wake Effect on Rotor Airloads and Performance.* NASA CR- 3726, 1983.

6. Hardin, J. C.; and Mason, J. P.: A New Look at Sound Generation by Blade/Vortex Interaction. *Trans. ASME, J. Vib., Acoust., Stress, & Reliab. Design*, vol. 107, Apr. 1985, pp. 224–228.

7. Hardin, Jay C.; and Lamkin, Stanley L.: Aeroacoustic Interaction of a Distributed Vortex With a Lifting Joukowski Airfoil. AIAA-84-2287, Oct. 1984.

8. Booth, Earl R., Jr.; and Yu, James C.: Two Dimensional Blade-Vortex Interaction Flow Visualization Study. AIAA-84-2307, Oct. 1984.

9. Commerford, G. L.; and Carta, F. O.: Unsteady Aerodynamic Response of a Two-Dimensional Airfoil at High Reduced Frequency. *AIAA J.*, vol. 12, no. 1, Jan. 1974, pp. 43–48.

10. Ziada, Samir; and Rockwell, Donald: Vortex-Leading-Edge Interaction. *J. Fluid Mech.*, vol. 118, May 1982, pp. 79–107.

11. Theodorsen, Theodore: *General Theory of Aerodynamic Instability and the Mechanism of Flutter.* NACA Rep. 496, 1935.

12. Sears, William R.: Some Aspects of Non-Stationary Airfoil Theory and Its Practical Application. *J. Aeronaut. Sci.*, vol. 8, no. 3, Jan. 1941, pp. 104–108.

13. Prandtl, L.: The Mechanics of Viscous Fluids. *Aerodynamic Theory*, div. G, Volume III, William Frederick Durand, ed., Durand Reprinting Committee, 1943, pp. 2–208.

14. Hubbard, Harvey H.; and Manning, James C.: *Aeroacoustic Research Facilities at NASA Langley Research Center—Description and Operational Characteristics*. NASA TM-84585, 1983.
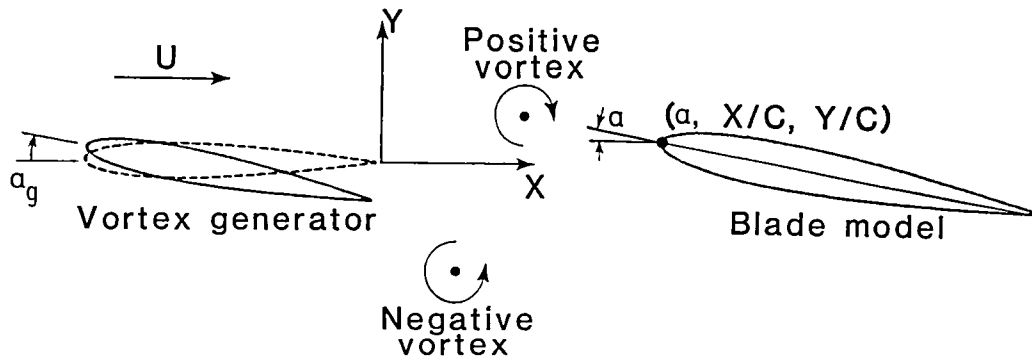
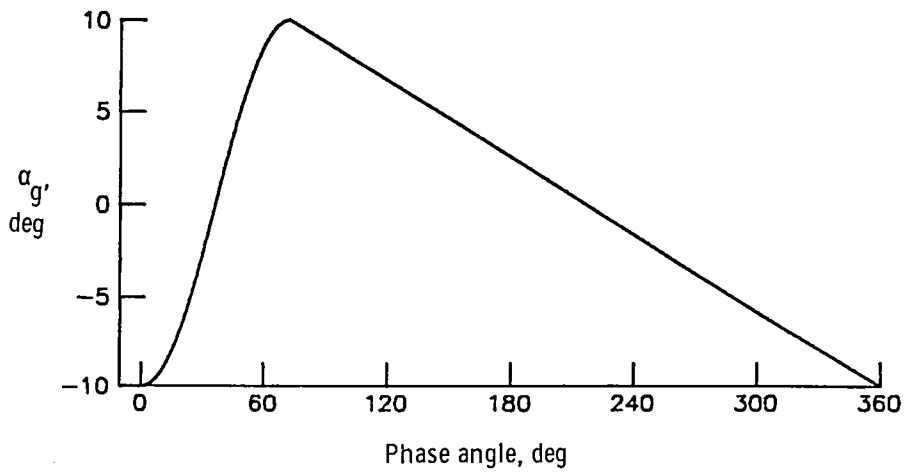Figure 1. Coordinate system used in study.
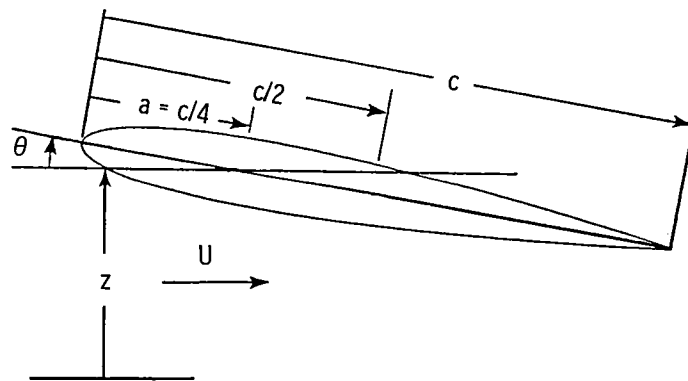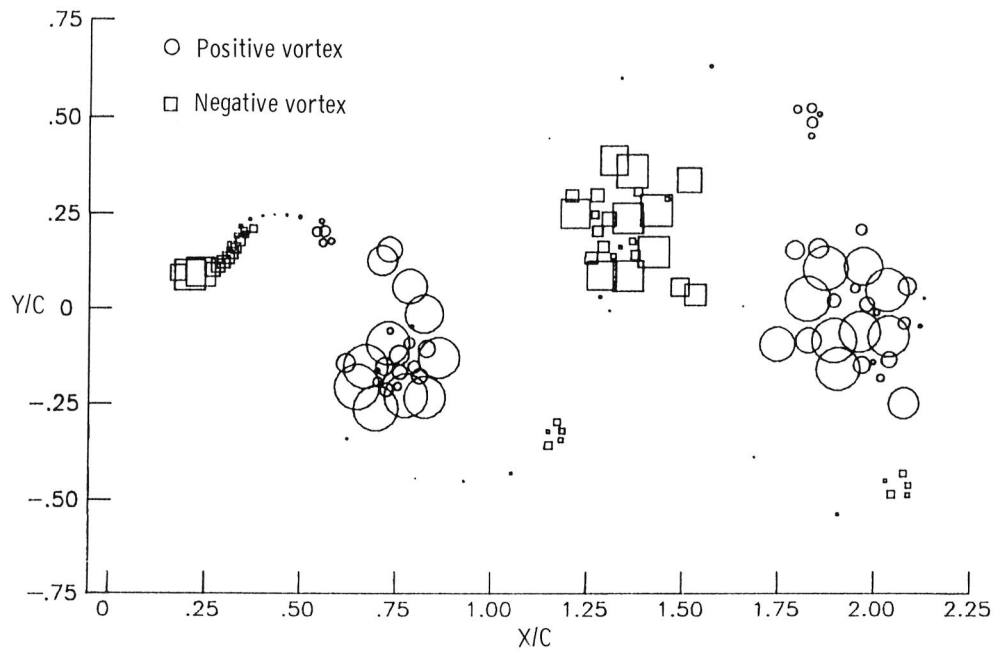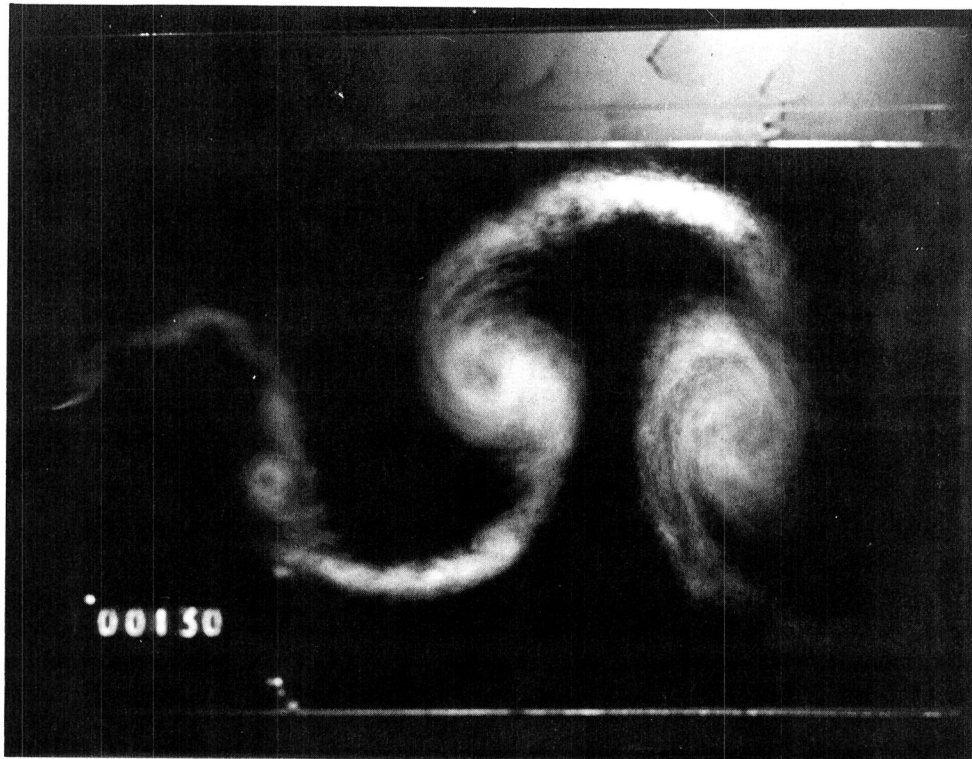

Figure 2. Pitch schedule for nonsinusoidal oscillation.

Figure 3. Geometry used to derive transient lift functions.

(a) Wake map.

L-85-178

(b) Flow visualization.

Figure 4. Comparison of computed wake structure and flow visualization for sinusoidal oscillation. Amplitude = 10°.
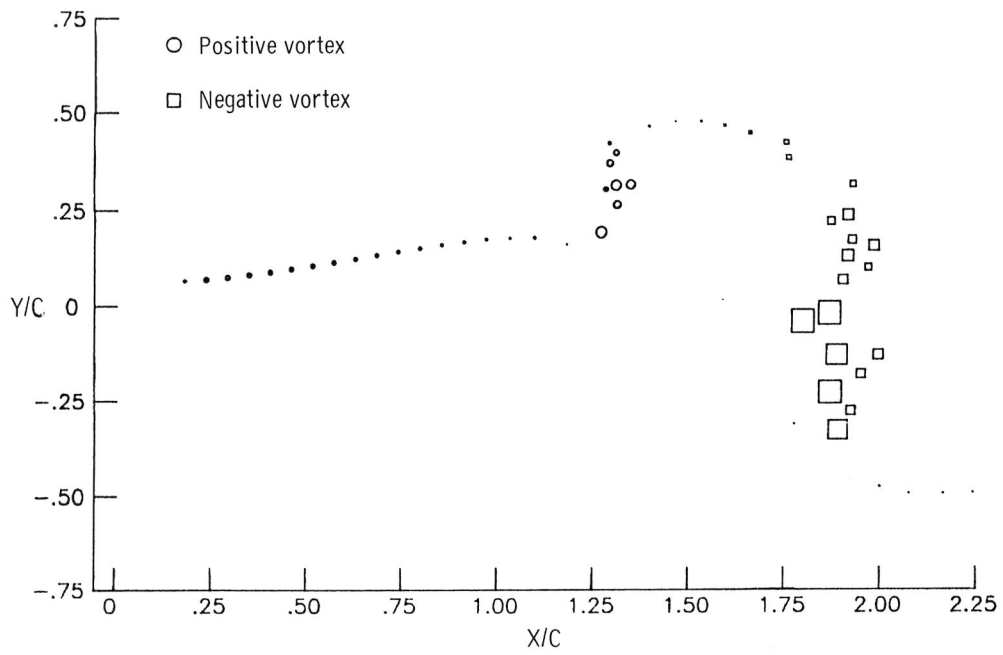
(a) Wake map.
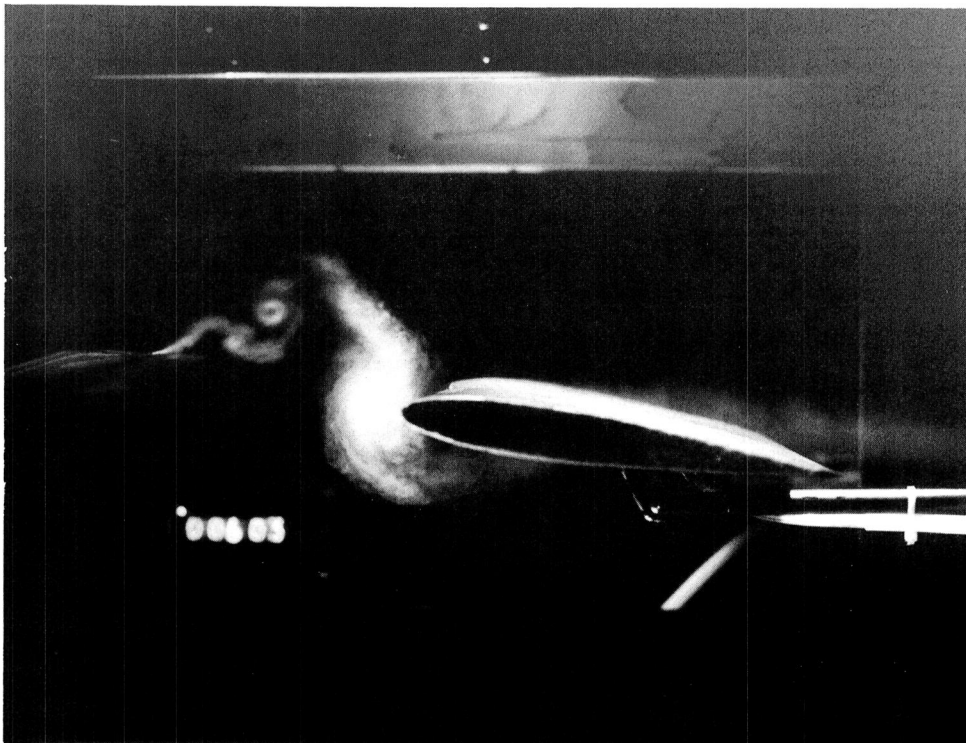
L-85-179

(b) Flow visualization.

Figure 5.   Comparison of computed wake structure and flow visualization for nonsinusoidal oscillation. Amplitude = 10°.

Camera
Equipment

Blade Model

Vortex Generator

Smoke
Generator

Support

Test Nozzle

4-ft-Diameter
Duct

Side View

Side Plate
with Window

Strobe Light

Sting/Traverse
System

Strobe Light

Front View
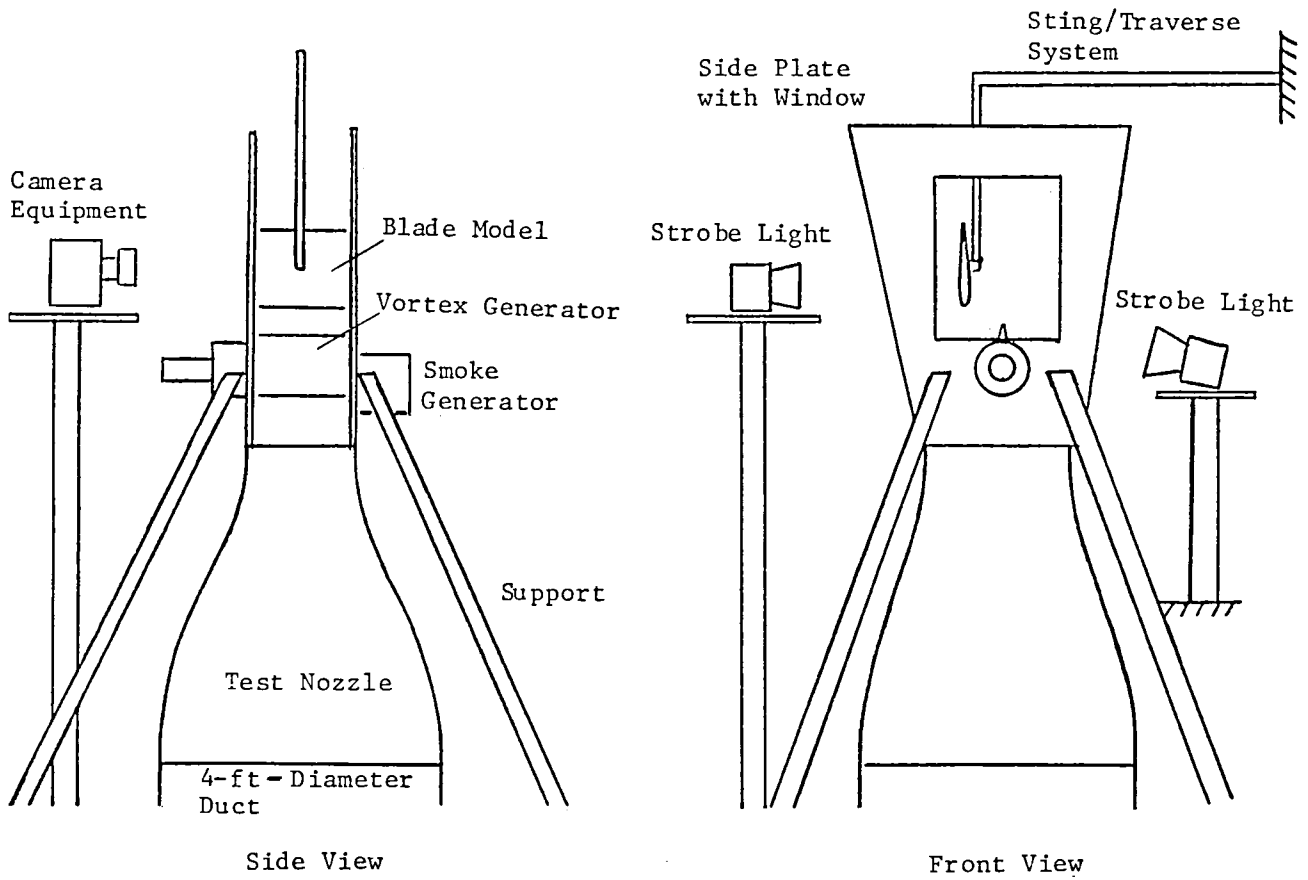
(a) Schematic diagram.

Figure 6. Test apparatus.
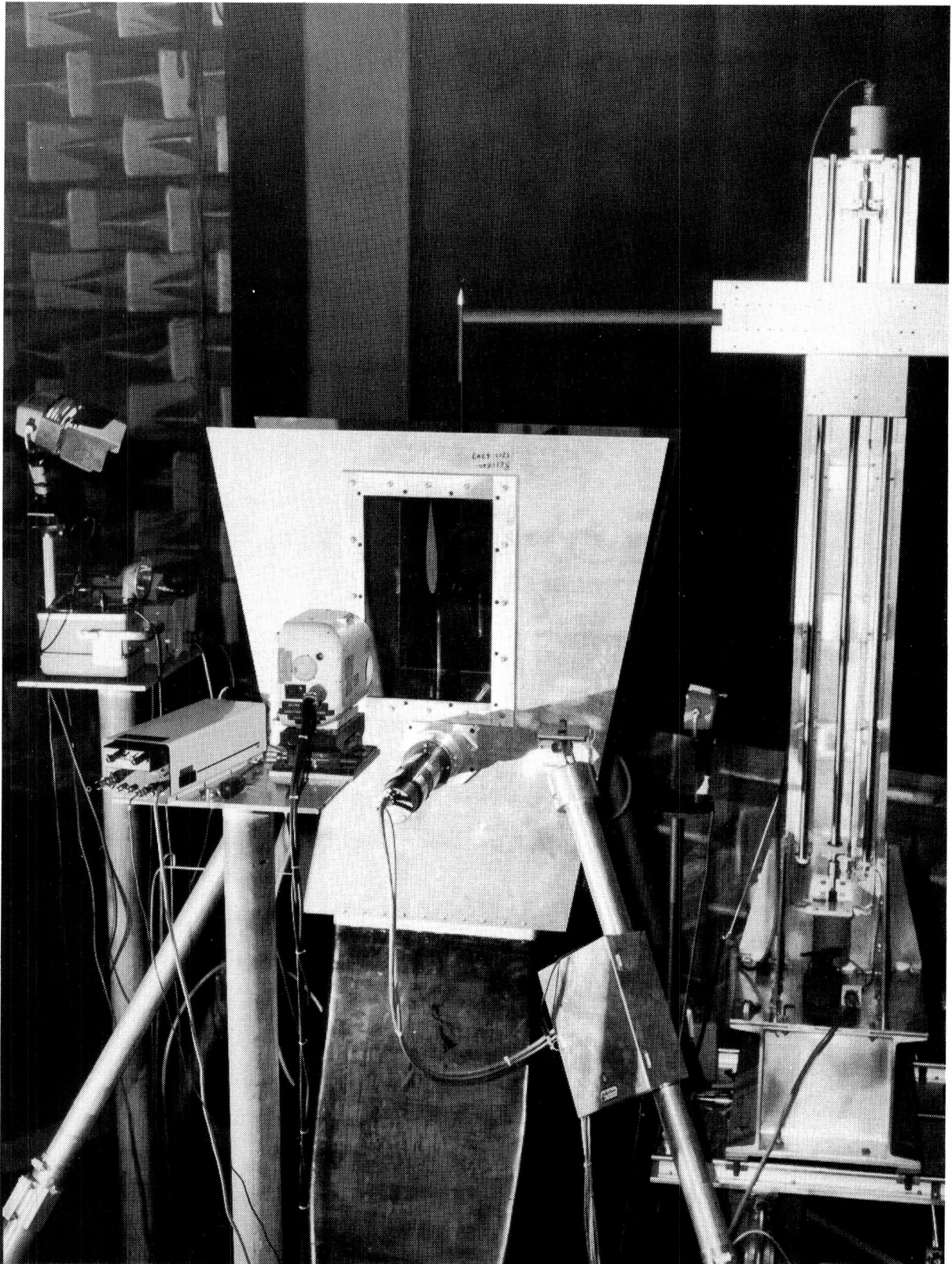
L-83-10,826

(b) Photograph.

Figure 6. Concluded.
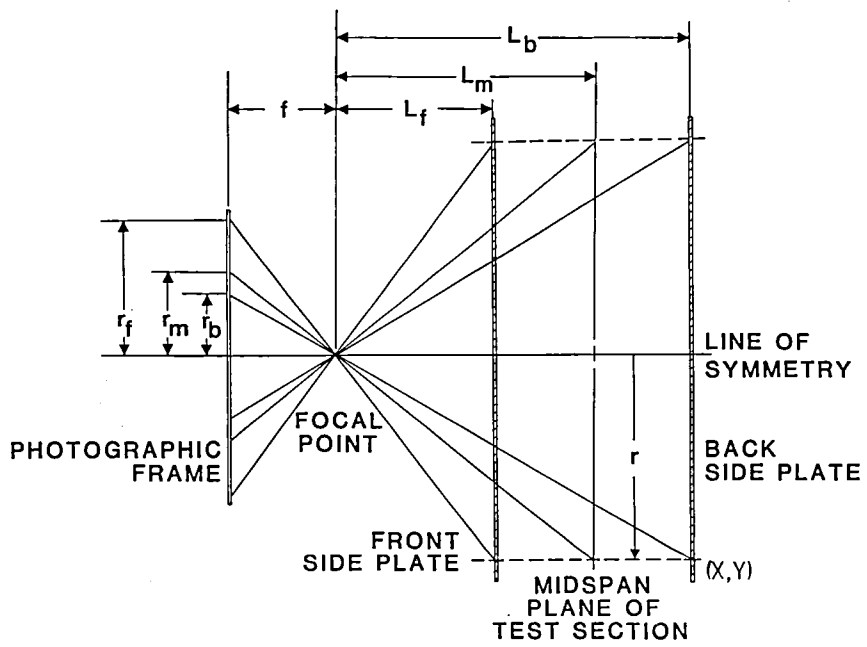
Figure 7. Schematic ray diagram for data reduction optical analysis.
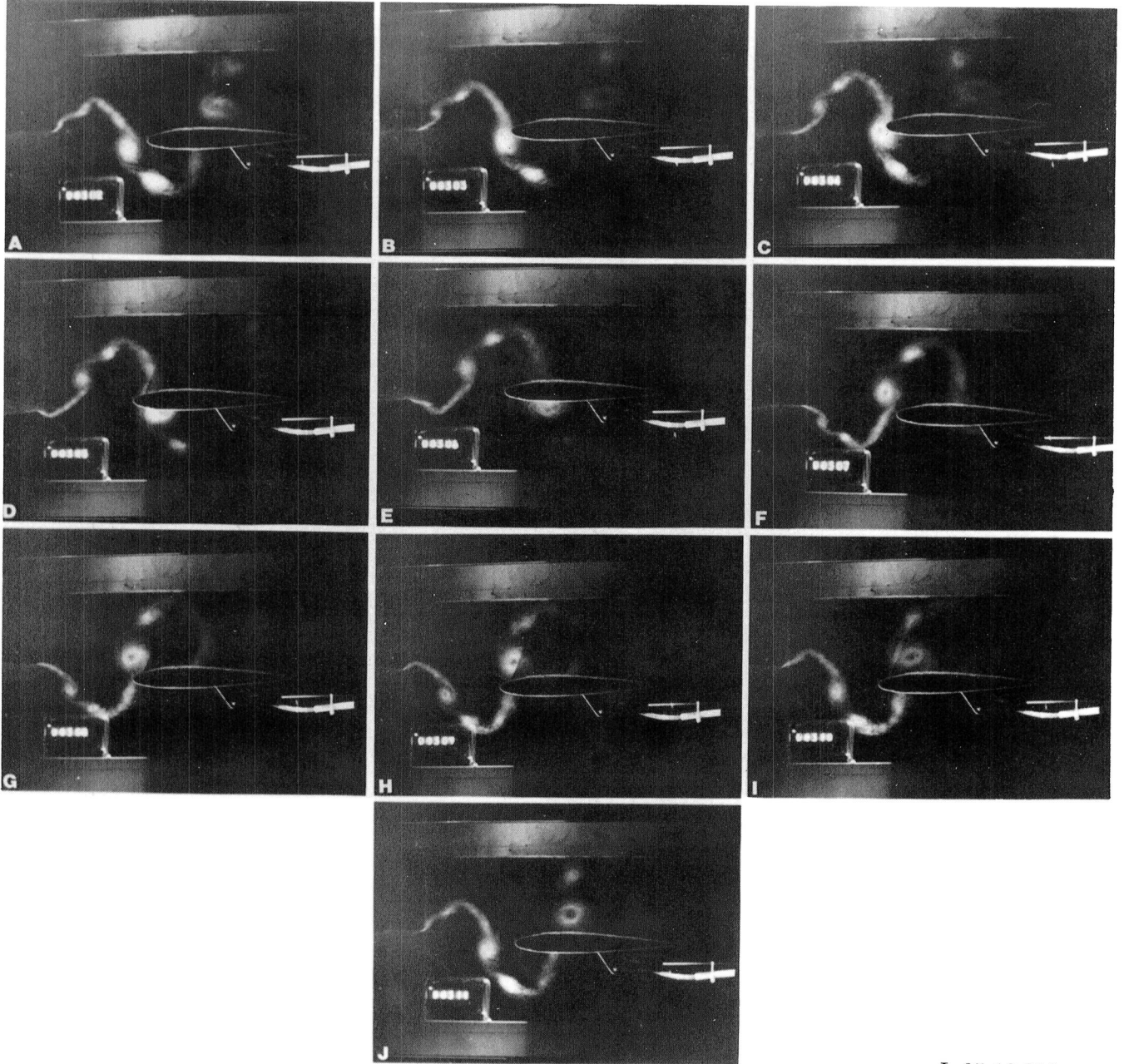
Figure 8. Sequence of phase-locked photographs for blade position $\alpha = 0°$; $X/C = 0.75$; $Y/C = 0.00$.
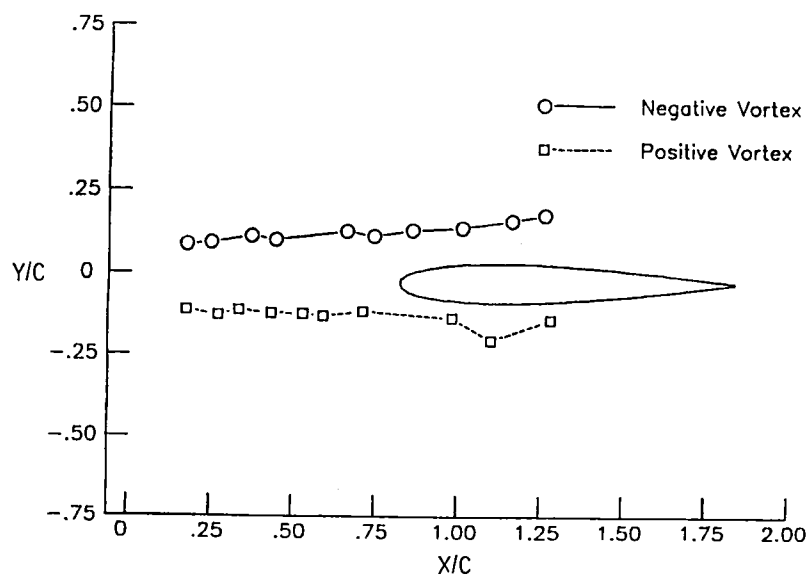
Figure 9. Vortex trajectory data obtained from photographs in figure 8.
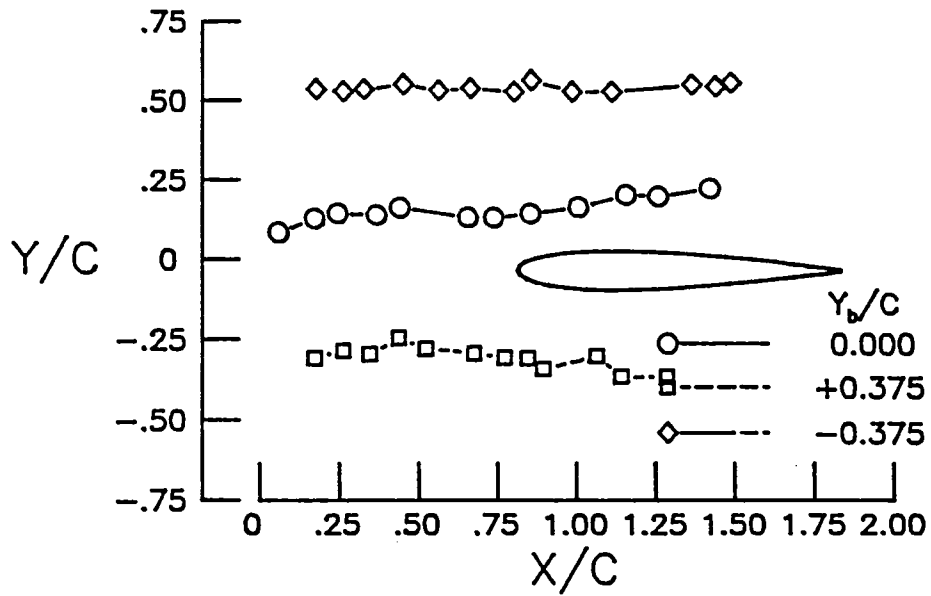
(a) Positive vortex.
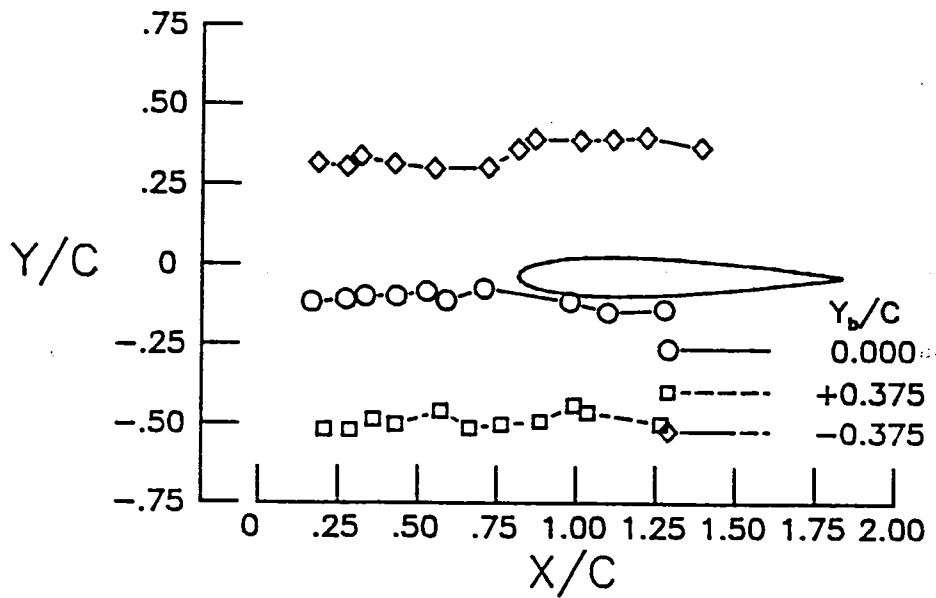
(b) Negative vortex.

Figure 10. Effect of blade vertical separation distance on vortex trajectory.
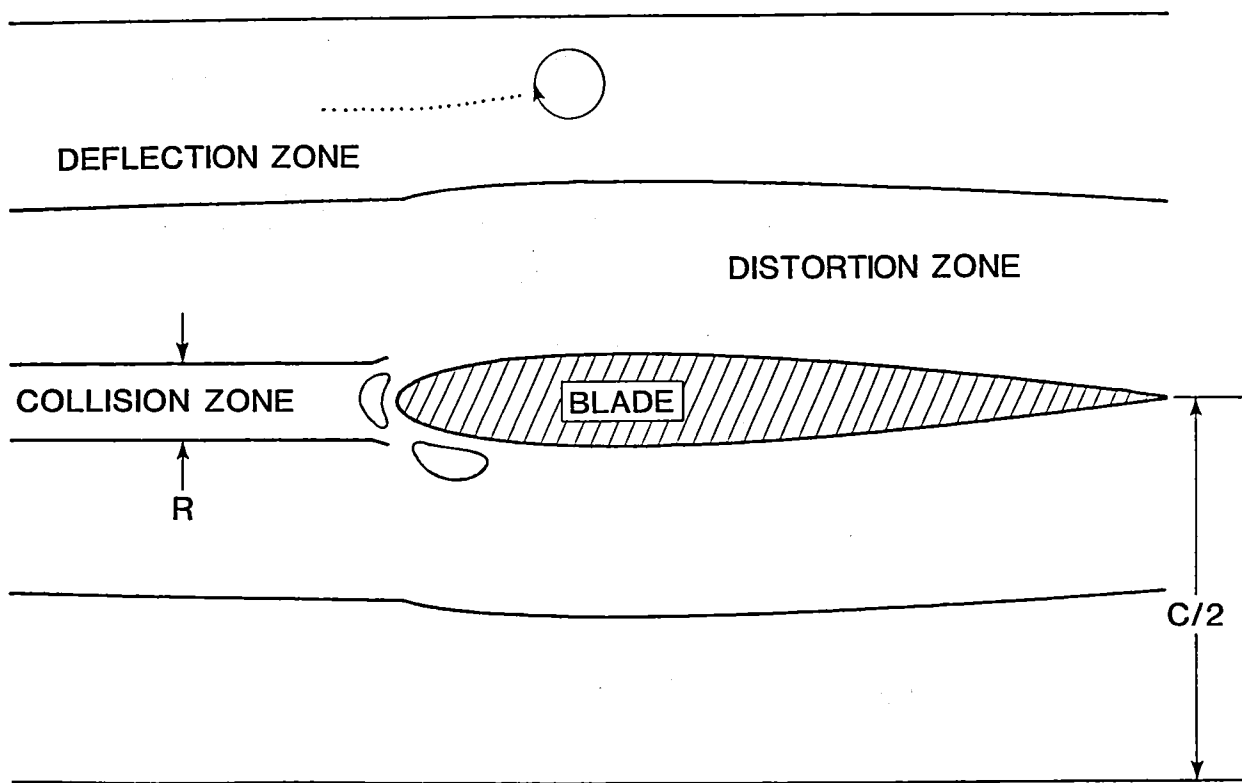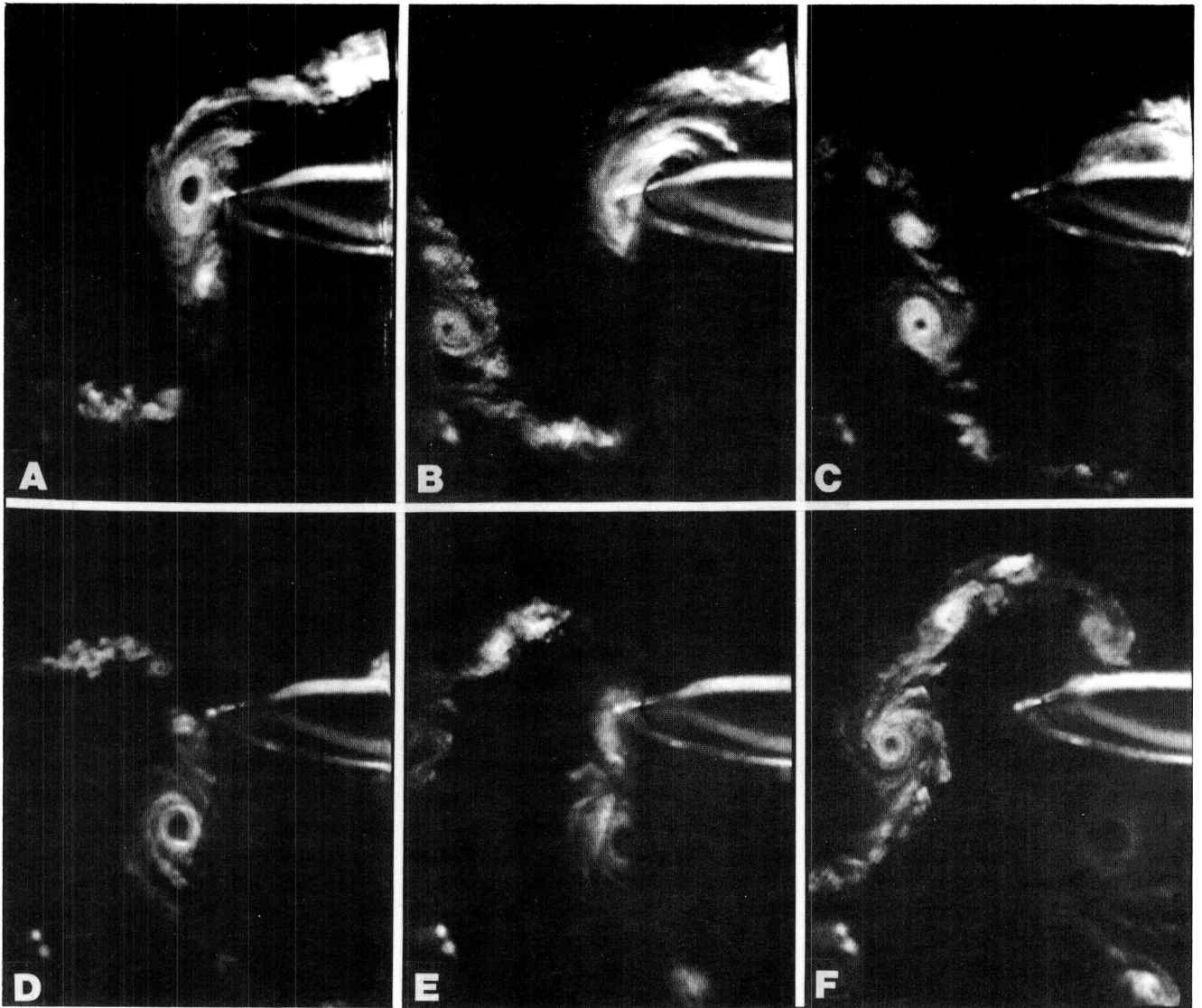
Figure 11. Characterization of blade-vortex interaction close encounter region into interaction zones.
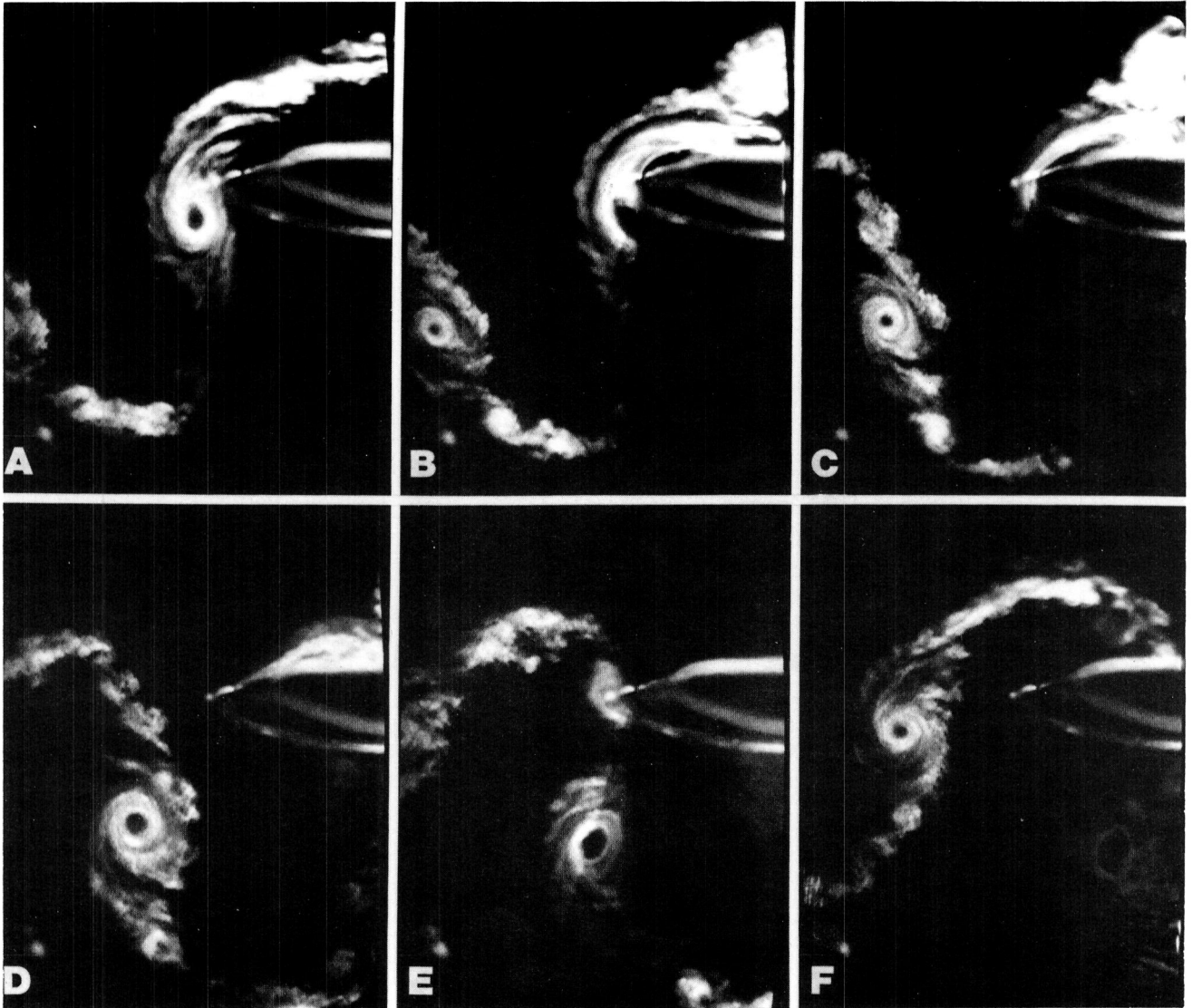
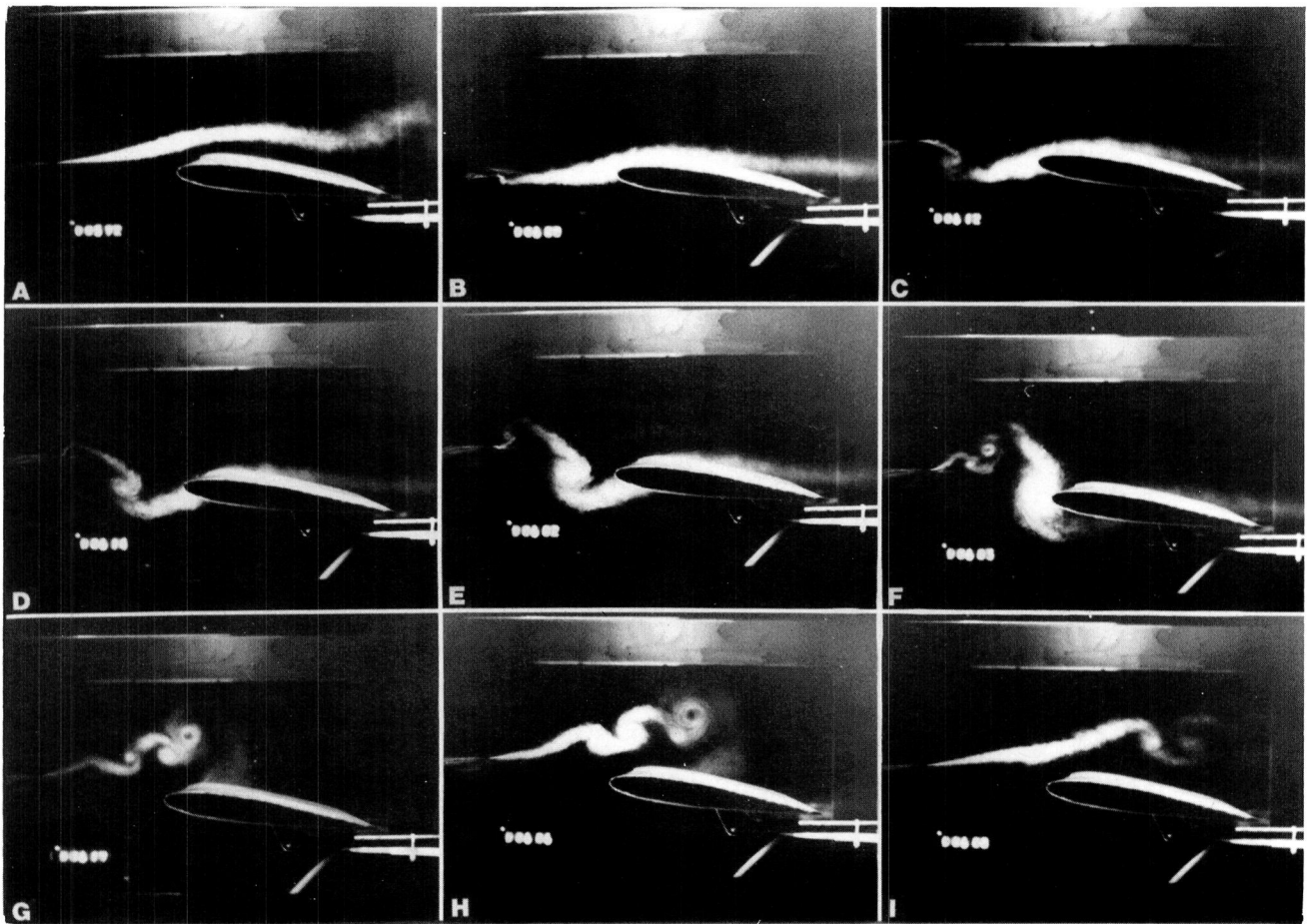Figure 12. Interaction of positive vortex with blade in deflection zone. $\alpha = 10°$; $X/C = 0.75$; $Y/C = 0.25$.

L-85-181

Figure 13. Interaction of positive vortex with blade in distortion zone. $\alpha = 10°$; $X/C = 0.75$; $Y/C = 0.219$.

22
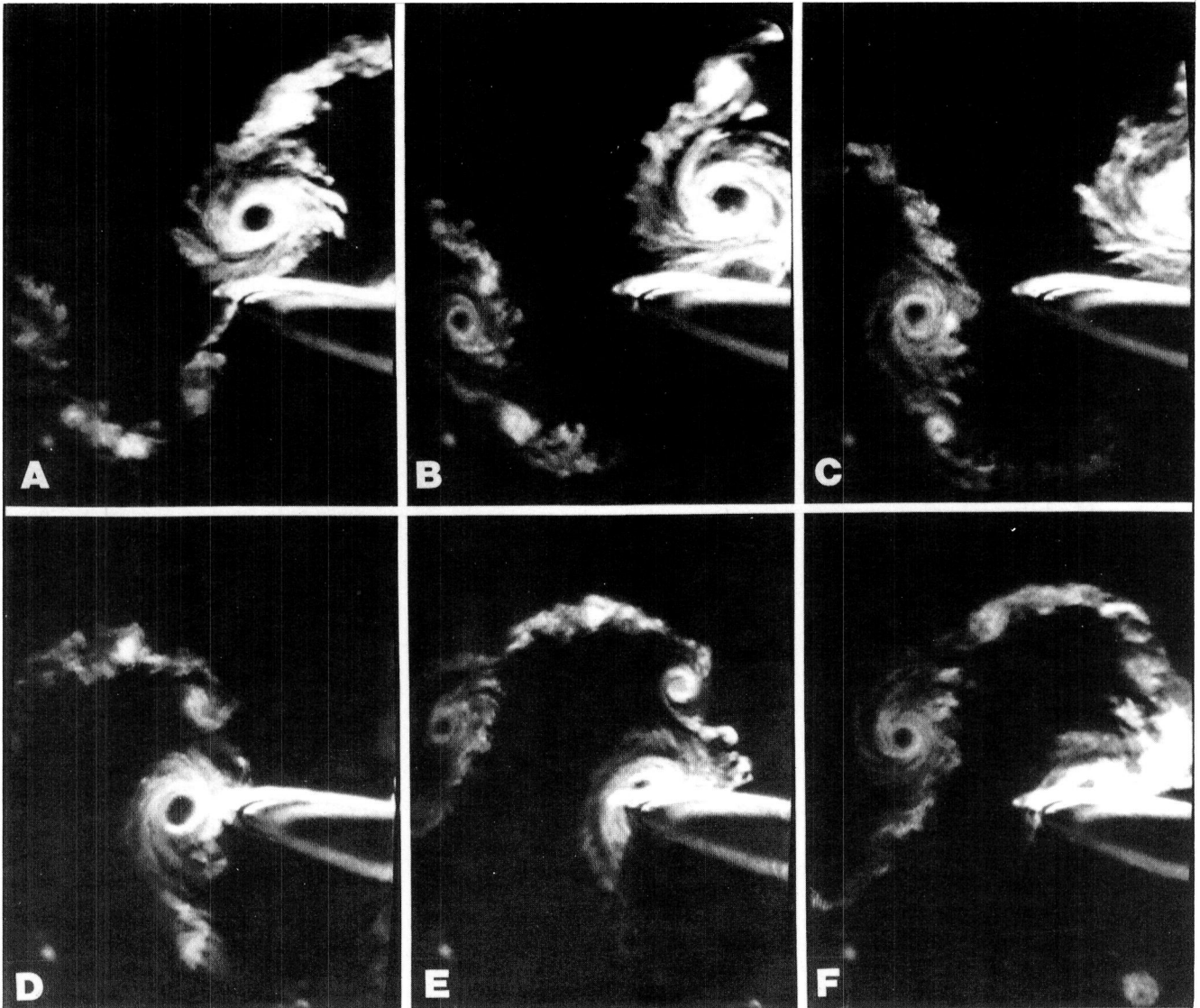
L-85-182

Figure 14. Interaction of positive vortex with blade in collision zone. $\alpha = 10°$; $X/C = 0.75$; $Y/C = 0.00$.

Figure 15. Flow visualization of blade in nonsinusoidal wake.
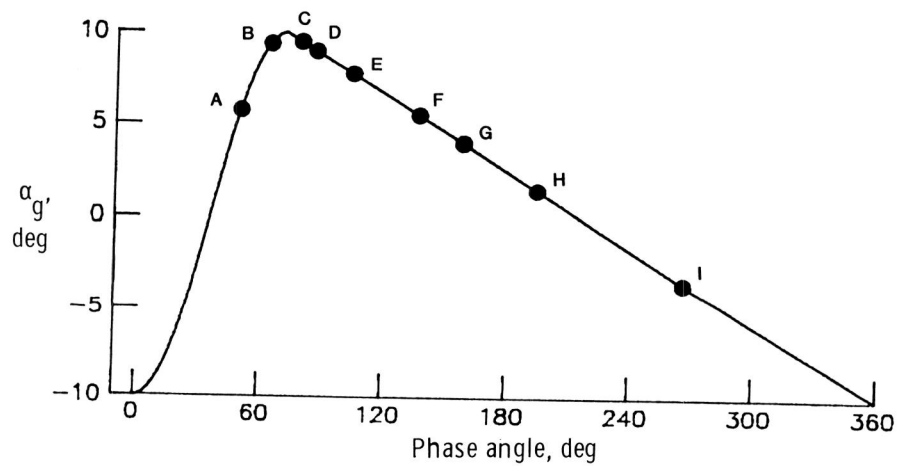
L-85-183

Figure 16. Pitch schedule for nonsinusoidal oscillation with labeled points corresponding to frames in figure 15.

1. Report No. NASA TP-2551	2. Government Accession No.	3. Recipient's Catalog No.
4. Title and Subtitle New Technique for Experimental Generation of Two-Dimensional Blade-Vortex Interaction at Low Reynolds Numbers		5. Report Date March 1986
		6. Performing Organization Code 505-61-51-06
7. Author(s) Earl R. Booth, Jr., and James C. Yu		8. Performing Organization Report No. L-15981
9. Performing Organization Name and Address NASA Langley Research Center Hampton, VA 23665-5225		10. Work Unit No.
		11. Contract or Grant No.
12. Sponsoring Agency Name and Address National Aeronautics and Space Administration Washington, DC 20546-0001		13. Type of Report and Period Covered Technical Paper
		14. Sponsoring Agency Code

15. Supplementary Notes

16. Abstract

An experimental investigation of two-dimensional blade-vortex interaction was initiated at NASA Langley Research Center. The first phase of this investigation was a flow visualization study to document the approach process of a two-dimensional vortex as it encountered a loaded blade model. To accomplish the flow visualization study, a method for generating two-dimensional vortex filaments was required. This report documents the numerical study used to define a new vortex generation process and the use of this process in the flow visualization study. Additionally, photographic techniques and data analysis methods used in the flow visualization study are examined.

17. Key Words (Suggested by Authors(s)) Blade-vortex interaction Two-dimensional vortex generation Unsteady aerodynamics Flow visualization	18. Distribution Statement Unclassified—Unlimited Subject Category 71		
19. Security Classif.(of this report) Unclassified	20. Security Classif.(of this page) Unclassified	21. No. of Pages 25	22. Price A02

National Aeronautics and
Space Administration
Code NIT-4

Washington, D.C.
20546-0001

LANGLEY RESEARCH CENTER

3 1176 01321 3898

RATE
FEES PAID
SA
Permit No. G-27

NASA